buildings

MDPI

Article

Intelligent Inspection Method for Rebar Installation Quality of Reinforced Concrete Slab Based on Point Cloud Processing and Semantic Segmentation

Ruishi Wang, Jianxiong Zhang, Hongxing Qiu * and Jian Sun

School of Civil Engineering, Southeast University, Nanjing 211189, China; 220221214@seu.edu.cn (R.W.); 230218697@seu.edu.cn (J.Z.); sunjian@seu.edu.cn (J.S.)
* Correspondence: qhx101000854@163.com

Abstract: The rebar installation quality significantly impacts the safety and durability of reinforced concrete (RC) structures. Traditional manual inspection is time-consuming, inefficient, and highly subjective. In order to solve this problem, this study uses a depth camera and aims to develop an intelligent inspection method for the rebar installation quality of an RC slab. The Random Sample Consensus (RANSAC) method is used to extract point cloud data for the bottom formwork, the upper and lower rebar lattices, and individual rebars. These data are utilized to measure the concrete cover thickness, the distance between the upper and lower rebar lattices, and the spacing between rebars in the RC slab. This paper introduces the concept of the "diameter calculation region" and combines point cloud semantic information with rebar segmentation mask information through the relationship between pixel coordinates and camera coordinates to measure the nominal diameter of the rebar. The verification results indicate that the maximum deviations for the concrete cover thickness, the distance between the upper and lower rebar lattices, and the spacing of the double-layer bidirectional rebar in the RC slab are 0.41 mm, 1.32 mm, and 5 mm, respectively. The accuracy of the nominal rebar diameter measurement reaches 98.4%, demonstrating high precision and applicability for quality inspection during the actual construction stage. Overall, this study integrates computer vision into traditional civil engineering research, utilizing depth cameras to acquire point cloud data and color results. It replaces inefficient manual inspection methods with an intelligent and efficient approach, addressing the challenge of detecting double-layer reinforcement. This has significant implications for practical engineering applications and the development of intelligent engineering monitoring systems.

Keywords: installation quality; rebar lattice; 3D sensor; point cloud processing; semantic segmentation

Citation: Wang, R.; Zhang, J.; Qiu, H.; Sun, J. Intelligent Inspection Method for Rebar Installation Quality of Reinforced Concrete Slab Based on Point Cloud Processing and Semantic Segmentation. *Buildings* **2024**, *14*, 3693. https://doi.org/10.3390/buildings14113693

Academic Editor: Vipul Patel

Received: 16 October 2024
Revised: 7 November 2024
Accepted: 8 November 2024
Published: 20 November 2024

1. Introduction

In concrete construction, the installation of substantial quantities of rebar is critical, as its quality directly influences structural safety and durability. Due to the extensive amount of rebar, quality inspections are predominantly conducted through manual sampling methods, which present several challenges: (1) significant time and labor costs due to the repetitive nature of the inspections; (2) the necessity for inspectors to access incomplete and potentially hazardous structures; and (3) the risk of reduced inspection standards or selective assessment, where only portions meeting the standards are verified while non-compliant parts may be disregarded. The third issue is particularly concerning, as defects in rebar installation may remain undetected until concrete placement, potentially leading to severe engineering failures, substantial injuries, and considerable financial losses. Therefore, advancing intelligent quality inspections in construction is one of the industry's development directions, which is crucial for improving the construction quality. The intelligent detection process for rebar installation involves addressing challenges in data acquisition, semantic segmentation, and point cloud processing.

The continuous innovation of computer vision technology has driven development in fields such as medical imaging [1,2], autonomous driving [3,4], augmented reality [5,6], and 3D modeling [7,8]. To obtain the 3D information of the object, depth cameras or target-based methods are commonly used to acquire the object's absolute dimensions. Yuan et al. [9] used a handheld laser scanner to inspect the installation positions of bridge rebars. Kim et al. [10] utilized terrestrial laser scanning (TLS) to scan the rebar and proposed a method for detecting the spacing and diameter of rebar lattices based on dense point clouds. Chang et al. [11] employed Structure from Motion and Multi-View Stereo (SFM-MVS) technology to reconstruct 3D point cloud models of column rebar cages and a single-layer rebar lattice using target-based methods to recover the absolute dimensions. Wang et al. [12] utilized colored laser scanning and extracted the rebar point clouds from the precast concrete component's raw point clouds and estimated the rebar hooks' position. Although a laser scan demonstrates significant advantages in data collection due to its high precision, including capturing detailed rib heights of the rebar [10], data collection is slow, requires high computational power, has high equipment costs, complex deployment, and relies on supporting structures. Target-based methods have limitations due to their high dependence on target placement and inability to directly measure key parameters such as the cover thickness and bottom-layer rebar diameter. Therefore, the 3D information acquisition methods using TLS and targets are more suitable for prefabrication factories, but it is challenging to meet the quality inspection needs of rebar installation on construction sites.

With the continuous advancement of computer vision, deep learning, and semantic segmentation, these artificial intelligence (AI) technologies are increasingly applied in civil engineering research. These technologies have compensated for the deficiencies of traditional image processing techniques, such as threshold segmentation [13], edge detection [14,15], and morphological processing [16] in practical engineering applications. They are gradually being applied to damage identification [17–19], deformation detection [20,21], component recognition [22,23], and mechanical performance prediction regression [24]. By applying semantic segmentation models to rebar installation inspection and acceptance processes, Yurii et al. [25] used the Mask R-CNN model for rebar detection, assisting a stereo camera in measuring the length, spacing, and diameter of a single-layer rebar lattice. Xin et al. [26] employed different semantic segmentation models to identify rebar surface corrosion. Xi et al. [27] utilized the Faster-RCNN model to detect rebar spacers in precast component factories. Currently, research on semantic segmentation for the rebar lattice installation quality is limited to single-layer rebars, as using semantic segmentation alone cannot distinguish between upper and lower layers. Thus, the post-segmentation measurement method for the diameter is not suitable for the quality of double-layer rebar lattices' installation inspection.

This study focuses on employing intelligent methods to inspect the rebar installation quality in RC slabs. The method integrates 3D point cloud data and 2D image information through the camera and the pixel coordinate system's transformations. This approach enables the inspection of the rebar installation quality for double-layer rebar lattices.

Section 2 describes the acquisition of point cloud data and the generation of rebar masks using semantic segmentation networks. Section 3 applies the RANSAC [28] method to process the point clouds, including tasks such as removing bottom formwork point clouds, separating upper and lower rebar lattices, and extracting individual rebars. Directly extracting semantic information from point clouds enables the measurement of the cover thickness, the distance between the upper and lower rebar lattices, and the spacing of double-layer bidirectional rebars. Additionally, rebar diameters are determined by integrating rebar masks with the semantic information from the point clouds. Section 4 evaluates the effectiveness and accuracy of the proposed algorithm using practical rebar grid examples.

2. Rebar Segmentation Based on Deep Learning

2.1. Data Acquisition

Data acquisition mainly includes two parts: point cloud acquisition of the tested object and image acquisition for the rebar segmentation dataset. The rebar segmentation dataset is used to train the semantic segmentation model to generate rebar masks. The main functions of the point cloud are as follows:

- In Sections 3.1 and 3.2, it is used to determine the thickness of the concrete cover, the distance between the upper and lower rebar lattices, and the spacing between double-layer bidirectional rebars through semantic information analysis;
- In Section 3.3, by converting between pixel data and point cloud data, it is possible to ascertain whether each rebar in the mask belongs to the upper or lower layer and to obtain the projection of the rebar axes onto the mask.

Data are acquired using the structured light camera ORBBEC Gemini 2 (Figure 1). The camera projects structural light patterns through a laser projector and captures images with two infrared cameras for stereo imaging to generate a depth image. Through calibration, it finally aligns the RGB image with the depth image on a pixel level.

Figure 1. ORBBEC Gemini 2 Camera.

As shown in Figure 2, O-XYZ represents the camera coordinate system, with O being the origin and (x, y, z) representing the coordinate of a point on the tested object's surface. The blue plane represents the imaging plane of the camera, with the pixel coordinate (u, v) on this plane. s_x, s_y represent the number of pixels per unit distance, and f represents the focal length, $f_x = f \cdot s_x$ and $f_y = f \cdot s_y$. According to the pinhole camera model, the transformation relationship from the point cloud coordinates to pixel coordinates is given by Equation (1). Conversely, the coordinate (x, y, z) of a point on the object's surface can also be calculated inversely using Equation (1), when giving the pixel coordinate (u, v) and depth information z.

$$\begin{bmatrix} u \\ v \\ 1 \end{bmatrix} = \frac{1}{z} \begin{bmatrix} f_x & 0 & c_x \\ 0 & f_y & c_y \\ 0 & 0 & 1 \end{bmatrix} \begin{bmatrix} x \\ y \\ z \end{bmatrix} \tag{1}$$

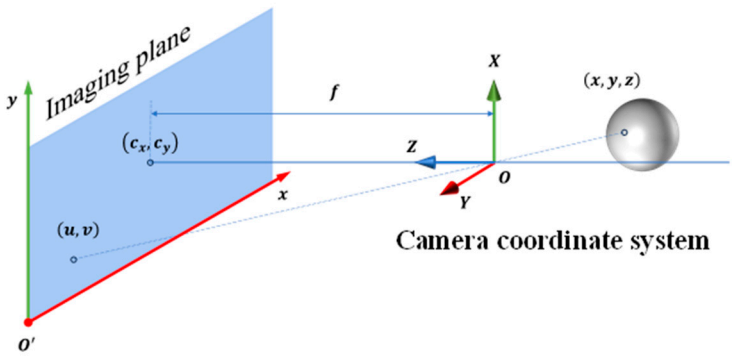

Figure 2. Point in O-XYZ to pixel in Imaging plane.

In order to conserve computational resources, it is required to remove environmental noise and reduce the point cloud density by applying statistical filtering and voxel grid downsampling.

2.2. Creation of Rebar Segmentation Dataset RL-600

An on-site capture of 684 images was conducted to create the Rebar Lattice 600 (RL-600) dataset. The dataset includes images captured under different shooting distances, lighting conditions, and formwork colors to ensure the trained model generalizes well to various scenarios and avoids overfitting to a specific condition.

The dataset was labeled using Labelme software 5.4.1, producing ".json" files. The obtained data were processed to generate segmentation mask images (Figure 3). In these mask images, the white regions represent rebar, while the black regions represent the background. The dataset was divided into training, test, and validation sets with a ratio of 6:2:2. (Table 1).

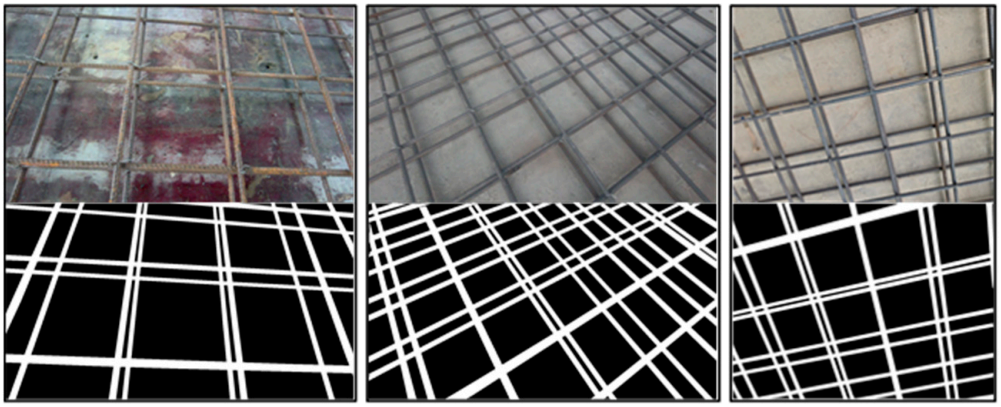

Figure 3. Semantic segmentation dataset.

Table 1. Division of dataset sample quantities.

	Images Number	Ratio
Train	410	60%
Test	137	20%
Validation	137	20%

2.3. Semantic Segmentation Model Training and Testing

In this section, U-Net, K-Net, and DeepLabV3+ were used to predict the rebar mask, the main function of which is to determine the boundaries of the rebar in Section 3.3.

2.3.1. Semantic Segmentation Model Introduction

U-Net [29] is widely used for the semantic segmentation of cells [30] and blood vessels [31] in medical imaging and has also been applied to crack detection in civil engineering [32–34], demonstrating its effective performance for "elongated" objects. K-Net [35] differs from classical CNN by employing dynamic convolution, where the convolutional kernels adapt based on input variations, which can help reduce the model's depth. K-Net has shown a strong performance in semantic, instance, and panoptic segmentation, providing a solid foundation for more efficient target recognition in subsequent applications within rebar engineering. DeepLabV3+ [36] enhances object boundary refinement, improving segmentation results and accuracy with significant clarity in boundary delineation. In rebar segmentation, this allows for precise boundary detection, facilitating accurate diameter calculations. Therefore, this study selects these three semantic segmentation models for predicting rebar masks and conducts a comparative analysis.

This study's semantic segmentation model and training weights are sourced from the Open-MMLab mmsegmentation toolkit. The training was performed on a Nvidia RTX 3090 GPU, using Python version 3.7, PyTorch version 1.10.0, and CUDA version 11.3.

2.3.2. Training Results

The performance of the three models was evaluated on the test set, which was completely unused during the training process. For single-class semantic segmentation, the task involves the binary classification of pixels into target and background categories. As shown in the confusion matrix in Table 2, pixel predictions are categorized as True (T) if correct and False (F) if incorrect. Pixels with true values of target are categorized as Positive (P), while those with true values of background are categorized as Negative (N). This results in four possible combinations: True Positive (TP), False Positive (FP), False Negative (FN), and True Negative (TN).

Table 2. Confusion matrix.

Predicted Values	Actual Values	
	Target	**Background**
Target	TP	FN
Background	FP	TN

The assessment of a model's performance mainly relies on the following metrics: ① Pixel Accuracy = (TP + TN)/(TP + TN + FP + FN), which represents the proportion of correctly predicted pixels out of all pixels. ② Dice = 2TP/(2TP + FP + FN)—the Dice coefficient is a measure of set similarity and is used to compare the similarity between the pixels predicted as targets and the actual target pixels. And, ③ IoU = TP/(TP + FP + FN), which represents the Intersection over Union (IoU) between the pixels predicted as targets and the actual target pixels.

Figure 4 shows the training process, presenting the variations of the Intersection over Union (IoU), Pixel Accuracy (PA), and Dice coefficient for the rebar regions. The graphs depict the evolution of these metrics when training and on the test set over the training steps. It can be observed that U-Net significantly underperforms compared to K-Net and DeepLabV3+ across all evaluated metrics. Conversely, although DeepLabV3+ shows metrics comparable to K-Net's, its performance on the test set exhibits greater fluctuations. This suggests that K-Net provides superior generalization capabilities, making it more effective for practical applications in construction sites.

As Table 3 shows, K-Net outperforms the other two models in all three evaluation metrics during the training process and on the test set. On the test set, K-Net achieves a PA of 97.74%, IoU of 93.37%, and a Dice coefficient of 96.51%. This superior performance is also evident from the actual mask generation results shown in Figure 5. Furthermore, as mentioned in Section 2.3.1, K-Net has demonstrated a remarkable performance in panoptic segmentation and instance segmentation, which provides the potential further expansion of this inspection process. Considering these factors, K-Net was chosen to predict rebar masks.

Table 3. Segmentation evaluation metrics.

Model	Train			Test		
	PA/%	**IoU/%**	**Dice/%**	**PA/%**	**IoU/%**	**Dice/%**
K-Net	95.89	90.33	94.79	97.74	93.37	96.53
U-Net	92.59	83.01	90.74	95.87	88.46	93.75
DeepLabV3+	95.74	88.74	94.14	97.91	92.58	95.59

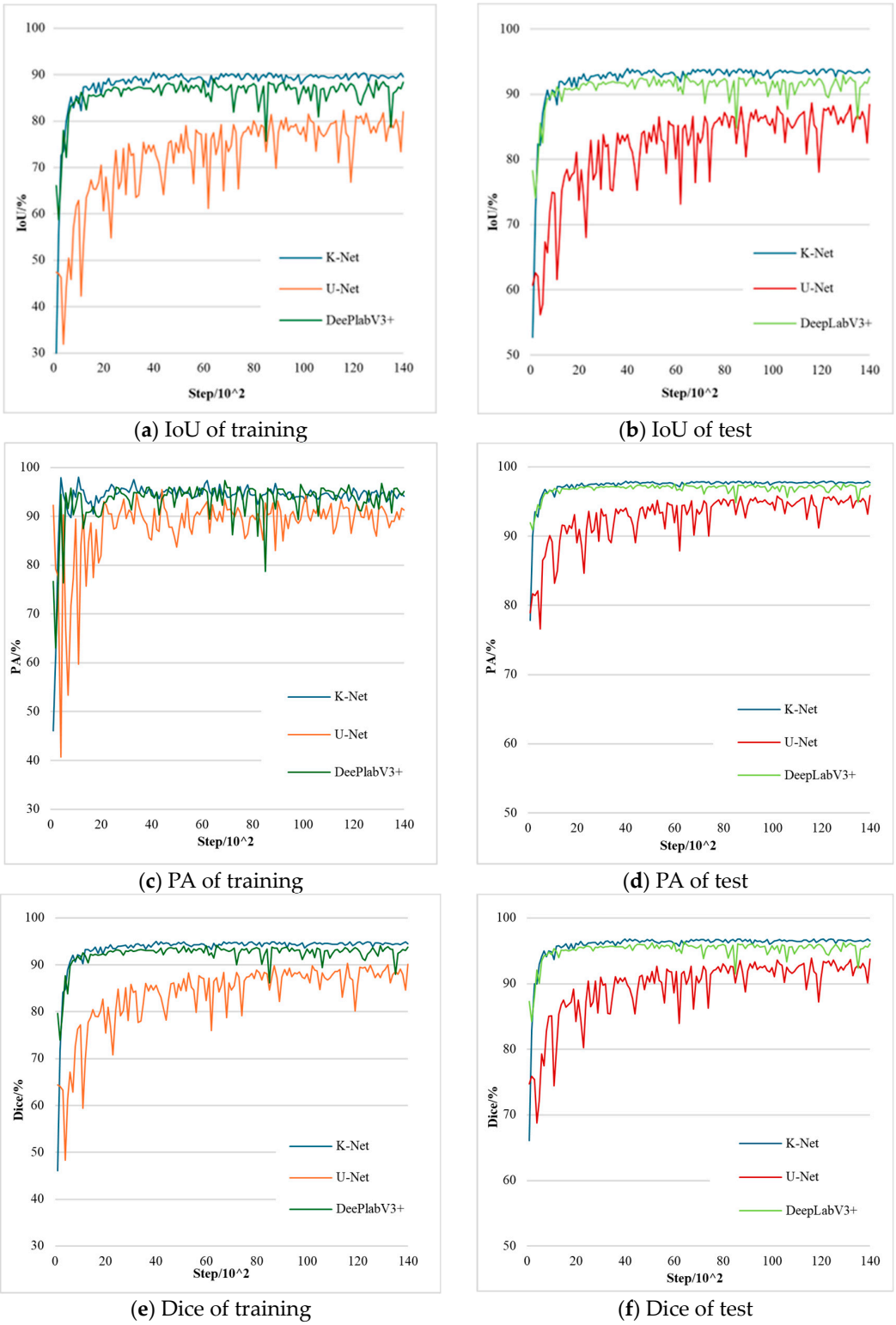

(**a**) IoU of training (**b**) IoU of test

(**c**) PA of training (**d**) PA of test

(**e**) Dice of training (**f**) Dice of test

Figure 4. Train and test processing.

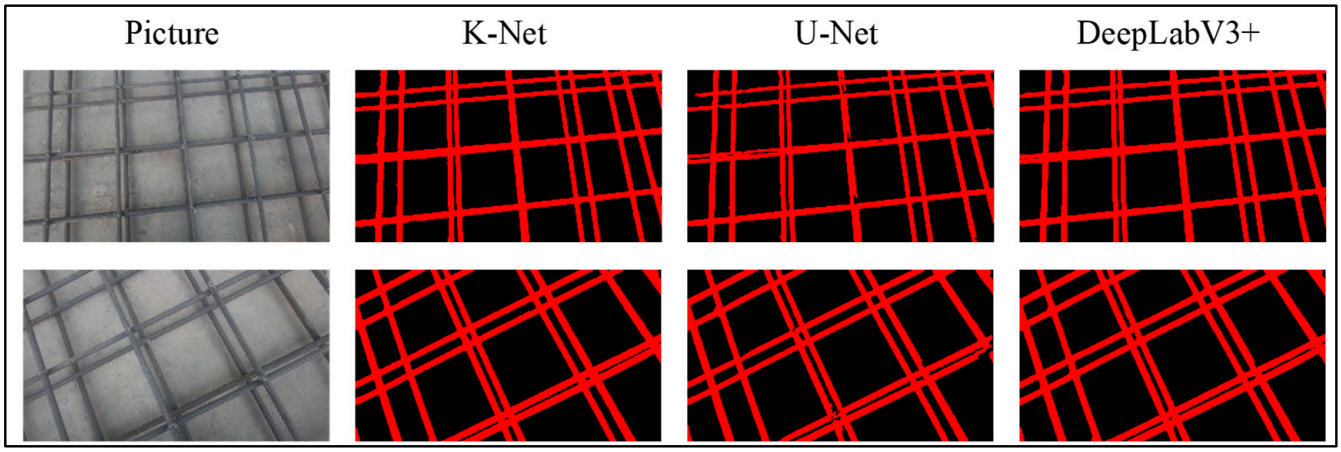

Figure 5. Segmentations of three models.

3. Inspection of Rebar Installation Deviations

Utilizing the reinforcement masks obtained in Section 2.3, Section 3 implements an intelligent inspection of the concrete cover thickness, the distance between the upper and lower rebar lattices, the spacing between the double-layer bidirectional rebar, and the nominal diameter of the rebar through point cloud processing algorithms. The inspection process comprises the following steps: In Section 3.1, the RANSAC method is used to fit the plane from the point cloud obtained in Section 2.1. The fitted plane enables the separation of the bottom formwork, upper rebar lattice, and lower rebar lattice and enables the measurement of the concrete cover thickness and the distance between the upper and lower rebar lattices. In Section 3.2, the RANSAC method is used to extract the individual rebar from each lattice. Subsequently, axis fitting is performed to measure the spacing between rebars. In Section 3.3, the fitted axes are projected onto the reinforcement masks obtained in Section 2.3 to distinguish whether the rebar in the masks belongs to the upper or lower layer. Then, specific point-pairs are identified for the diameter measurement within the diameter calculation region.

3.1. Concrete Cover Thickness and the Distance Between Upper and Lower Rebar Lattices

In the rebar installation quality inspection, the collected point cloud mainly consists of rebar, bottom formwork, and environmental noise. Among the collected point clouds, the number of bottom formwork point clouds significantly exceeds that of rebar points. Specifically, the bottom formwork point clouds account for about 75% of the total, while the rebar point clouds make up about 25%.

To achieve the rebar installation quality inspection, it is necessary to filter out the bottom formwork, which accounts for a large proportion and to extract the rebar individually for the following processing. Although the bottom formwork point clouds exhibit slight fluctuations because of inevitable noise during the data acquisition, and the data are in the form of a non-ideal plane, it is still approximately planar compared to the spatial position of the rebar point clouds. Therefore, adopting the RANSAC plane fitting method can effectively separate the bottom formwork point clouds from the initial point clouds.

The specific steps are as follows:

1. Randomly select three points from the point cloud data for plane fitting to obtain a plane $P_k(k = 1, 2, 3, \cdots)$ (as shown by the blue plane in Figure 6a);
2. Take the points whose distance from the fitting plane is less than the threshold t_1 as an "inline set"—t_1 is 0.8 times the design value of the concrete cover thickness;
3. Iterate step 1 and 2 and stop after k times;
4. The final chosen result is the bottom formwork plane, P_f(as shown by the green plane in Figure 6a) who has the most inline set, and the plane equation is $a_f x + b_f y + c_f z + d_f = 0$;

5. Delete the point clouds set belonging to the bottom formwork plane P_f to obtain the point clouds of the upper and lower rebar lattices (Figure 6b).

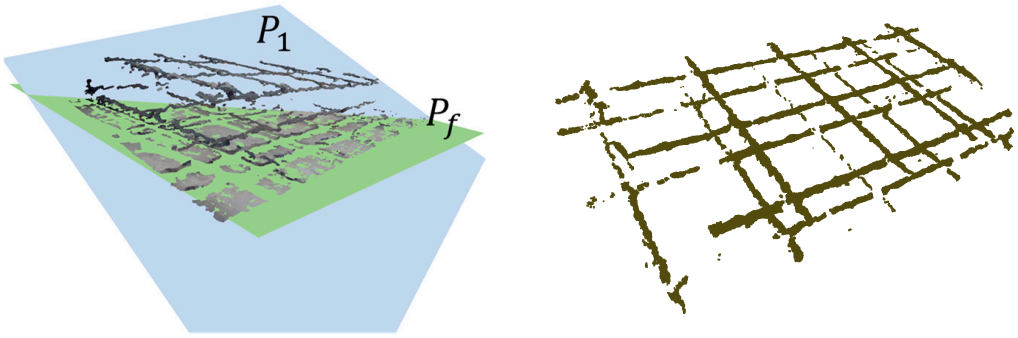

(**a**) RANSAC fitting plane (**b**) Point cloud of two rebar lattices

Figure 6. Point cloud processing 1.

The bottom formwork point clouds account for about 75% of the total. Among them, approximately 40% of the formwork point clouds can be used to fit the plane. The probability that there is at least one outlier among the sample points selected for each iteration of the model is $1 - 0.3^3$. When the number of iterations is k, the probability that there is at least one outlier sample in all iterations is $\left(1 - 0.3^3\right)^k$. The probability that there is at least one correct fit result of the k iterations is $P_R = 1 - \left(1 - 0.3^3\right)^k$. If a 99% P_R is wanted, then $k = \ln(1 - 0.99)/\ln\left(1 - 0.3^3\right) = 168.2$. Therefore, we set $k = 170$.

In order to avoid the upper rebar lattice blocking the lower rebar lattice and to ensure the complete acquisition of the point clouds, oblique shooting should be used when inspecting. However, oblique shooting will cause a certain angle between the normal vector of the bottom formwork plane and the Z-axis direction of the camera coordinate system, resulting in variations in the Z-coordinate values of point clouds on the same horizontal plane (as shown by the gray point cloud in Figure 7). To better distinguish the bottom formwork, lower rebar lattice, and upper rebar lattice point clouds on different horizontal planes using Z-coordinate values, the entire point cloud is first rotated according to Equation (3). This rotation also helps to save the computation time in subsequent processing. X is the point cloud coordinate matrix before rotation, and X' is the point cloud coordinate matrix after rotation. The rotation matrix is as shown in Equation (2): R_x is the rotation matrix of the point clouds around the X-axis and α is the angle between the projection of the normal of the plane P_f on the YOZ plane and the Z-axis; R_y is the rotation matrix of the point clouds around the Y axis and β is the angle between the projection of the normal of the plane P_f on the XOZ plane and the Z-axis. After rotation, the normal vector of the bottom formwork plane coincides with the Z-axis of the camera coordinate system, and the distance from the origin of the camera coordinate system to the new bottom formwork plane is $h_f = d_f / \left({a_f}^2 + {b_f}^2 + {c_f}^2\right)^{0.5}$.

$$R_x = \begin{bmatrix} 1 & 0 & 0 \\ 0 & cos\alpha & -sin\alpha \\ 0 & sin\alpha & cos\alpha \end{bmatrix} \; R_y = \begin{bmatrix} cos\beta & 0 & sin\beta \\ 0 & 1 & 0 \\ -sin\beta & 0 & cos\beta \end{bmatrix} \tag{2}$$

$$X' = R_x R_y X \tag{3}$$

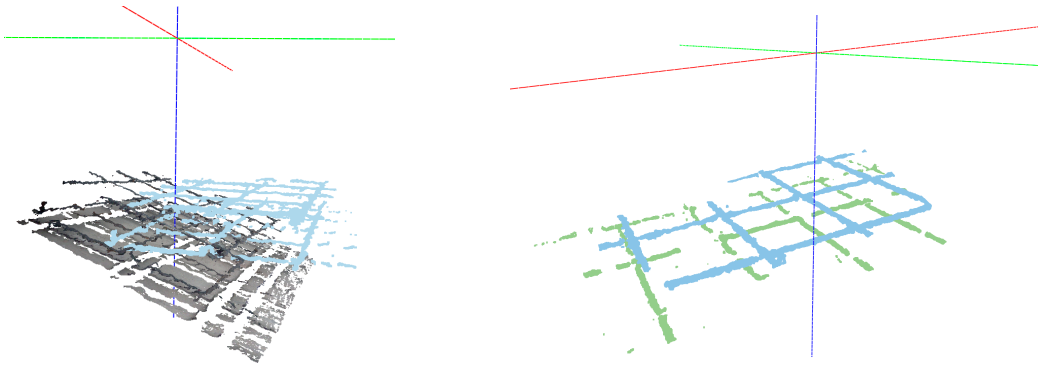

(**a**) Point cloud rotation (**b**) Separation of upper and lower rebar

Figure 7. Point cloud processing 2.

As shown in Figure 7b, after the upper and lower rebar lattices' point clouds are rotated, the Z-coordinates of points within the same lattice are nearly identical. Consequently, the upper and lower rebar lattices can be separated according to the range of Z-coordinates. The thickness of the concrete cover and the distance between the upper and lower rebar lattices can be calculated based on this. The specific steps are as follows:

1. Subtract the Z-coordinate value of each point from h_f; if $\left|z_i - h_f\right| < t_2 (i = 1, 2, 3, \cdots)$, it is classified as the lower rebar lattice (as shown by the green point cloud in Figure 7b), otherwise it is classified as the upper rebar lattice (as shown by the blue point cloud in Figure 7b), and the threshold value t_2 is generally set to 50 mm;
2. Randomly select the Z-coordinates $z_l (l = 1, 2, 3, \cdots, 1000)$ of 1000 points in the lower rebar lattice. Calculate the average value m_1 of $\left|z_l - h_f\right|$ and subtract 1.2 times the design value d_l of the rebar diameter of the lower layer to obtain the thickness of the concrete cover $c = m_1 - 1.2 d_l$.
3. Randomly select the Z-coordinates $z_u (u = 1, 2, 3, \cdots, 1000)$ of 1000 points in the upper rebar lattice. Calculate the average value m_2 of $\left|z_u - h_f\right|$, then obtain the distance $m_2 - m_1$ between the upper and lower rebar lattice.

3.2. Spacing of Double-Layer Bidirectional Rebar in RC Slab

In order to measure the spacing of the double-layer bidirectional rebar, it is necessary to extract the individual rebar point clouds from the upper and lower rebar lattices' point clouds obtained in Section 3.1. On the construction site, straightness errors may exist, caused by improper rebar installation and environmental noise during data acquisition. However, compared with the longitudinal length of the rebar, lateral coordinate errors in the rebar point clouds can be neglected. Therefore, each rebar point cloud can still be regarded as a straight line, and the RANSAC straight line fitting method can be used to extract the rebar point clouds individually. The specific steps are as follows:

1. Select two points in the current layer of rebar lattice point clouds for fitting the straight line $l_k (k = 1, 2, 3, \cdots)$ (Figure 8);
2. Take the points whose distance from the fitting straight line is less than threshold t_4 as an "inline set" (the dark point cloud on the left side of Figure 8). The threshold t_4 should be slightly larger than half of the design value of the rebar nominal diameter. Iterate step ①② for k times;
3. The final chosen result is l_{rebar} (Figure 8), who has the most "inline set" and is considered as the axis of the rebar. Use the points in the chosen "inline set" as the rebar point cloud (the dark point cloud on the right side of Figure 8);
4. To prevent repeated calculations, delete the rebar point cloud selected in step 3 from the current rebar lattice.

5. Repeat steps 1, 2, 3, and 4. When the number of remaining point clouds is less than 0.06 times the total number of point clouds of the current rebar lattice, the extraction of the single rebar point cloud is considered to be completed.

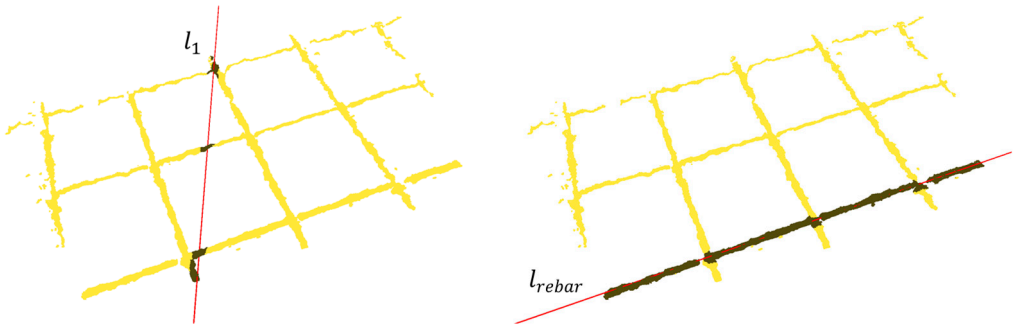

Figure 8. Individual rebar recognition.

The individual rebar point cloud account for about 10% of a rebar lattice layer. The probability that there is at least one outlier among the sample points selected for each iteration of the model is $1 - 0.1^2$. When the number of iterations is k, the probability that there is at least one outlier sample in all iterations is $\left(1 - 0.1^2\right)^k$. The probability that there is at least one correct fit result of the k iterations is $P_R = 1 - \left(1 - 0.1^2\right)^k$. If a 99% P_R is wanted, then $k = \ln(1 - 0.99)/\ln\left(1 - 0.1^2\right) = 458.2$. Therefore, we set $k = 460$.

Finally, check the number of rebar points. When the number of points on a certain rebar is less than 0.4 times the average number of point clouds on the current rebar lattice layer, it is considered that the point cloud of this rebar has not collected the 3D information well. In order to avoid errors in subsequent calculations that may affect the inspectors' judgment, this rebar point cloud needs to be deleted.

The rebar axis l_{rebar} obtained in Section 3.2 is Equation (4). In order to calculate the spacing of the double-layer bidirectional rebar, $\left(k_i^1, k_i^2\right)$ clustering is performed by the K-means algorithm [37]. The rebar point clouds need to be divided into two mutually perpendicular classes, so the number of classes is two. The specific method is as follows:

1. Randomly select two points as "class centers", calculate the distances from each point to the two class centers. Then classify each point into the class with a closer distance;
2. Recalculate the centroid of the two classes which are the new "class centers", recalculate the distance from each point to the new "class centers", and classify it into the class with a closer distance;
3. Iterate step 2 and stop after k times.

According to the elements in the two classes obtained at the end, the corresponding rebar fitted lines are divided into two mutually perpendicular line groups. Since the fitted straight line will not be completely parallel, select 1000 points randomly from the point set of one rebar and calculate the average distance from each point to the fitted axis of the other rebar. The average distance is considered as the spacing between two adjacent rebars.

$$\begin{cases} x = k_i^1 \times z + b_i^1 \\ y = k_i^2 \times z + b_i^2 \end{cases} (i = 1, 2, 3, \cdots) \tag{4}$$

3.3. Rebar Nominal Diameter

The point cloud data acquired by structured light cameras are sparser when compared to those captured by laser scanners. Moreover, because of the jitter that occurs during the mobile sampling process, the rebar point clouds more closely resemble a plane than a curved surface (Figure 9). So it is impossible to use RANSAC circle fitting or cylinder fitting to inspect the nominal diameter [28]. For this limitation, this paper uses the rebar segmentation mask obtained in Section 2.3 and the rebar point clouds to identify the rebar

diameter. The orange plane γ in Figure 9 is the imaginary plane, which is perpendicular to the plane formed by the rebar axis l_{rebar} obtained in Section 3.2 and the origin of the camera coordinate system $O(0,0,0)$. The intersection of the two planes is l_{rebar}.

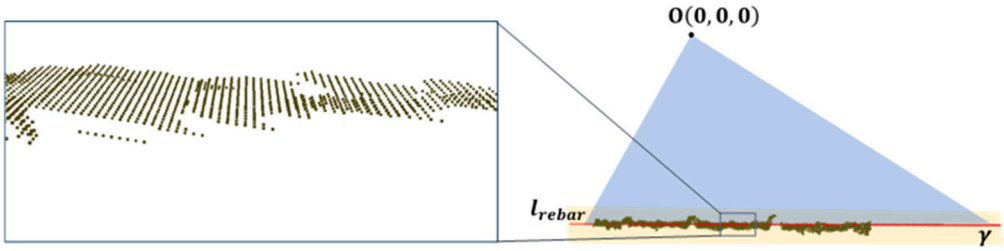

Figure 9. Rebar point cloud and imaginary plane.

In order to calculate the diameter, point-pairs perpendicular to the rebar axis l_{rebar} are found in rebar point clouds. Since the camera is tilted during data acquisition, the projection of the point-pair and the fitted line on the mask (imaging plane) may not remain perpendicular. The region framed in purple in Figure 10 is the rebar diameter calculation region. The projection slope k_m of the point-pair on the mask is also the long side slope of the parallelogram rebar diameter calculation region. In Section 3.2, we obtained the direction vector $\vec{v} = (l, m, n)$ of the rebar axis l_{rebar}. Within the rebar point clouds, find a point $\mathrm{p}(x_\mathrm{p}, y_\mathrm{p}, z_\mathrm{p})$ to be the detect-point as close to l_{rebar} as possible. Vector $\vec{\mathrm{pO}} = (x_\mathrm{p}, y_\mathrm{p}, z_\mathrm{p})$ is obtained by giving the origin of the camera coordinate system $O(0,0,0)$. The direction vector of the selected point-pair is $\vec{v_\mathrm{p}} = \vec{\mathrm{pO}} \times \vec{v} = (l_\mathrm{p}, m_\mathrm{p}, n_\mathrm{p})$. Equation (5) shows a line l_s passing through the point p with the direction vector $\vec{v_\mathrm{p}}$.

$$\frac{x - x_\mathrm{p}}{l_\mathrm{p}} = \frac{y - y_\mathrm{p}}{m_\mathrm{p}} = \frac{z - z_\mathrm{p}}{n_\mathrm{p}} \tag{5}$$

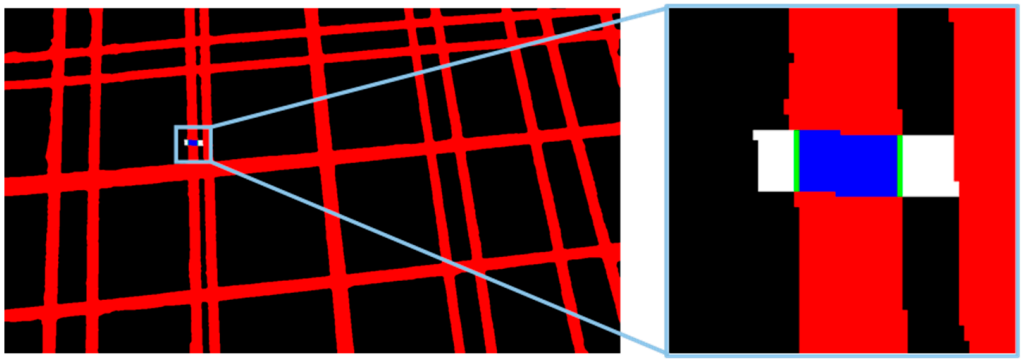

Figure 10. Rebar Diameter calculation region.

The pixel coordinate on the mask of p is $pixel_\mathrm{p}(u_\mathrm{p}, v_\mathrm{p})$, and there is another point $\mathrm{q}(x_\mathrm{p} + l_\mathrm{p}, y_\mathrm{p} + m_\mathrm{p}, z_\mathrm{p} + n_\mathrm{p})$ on l_s whose pixel coordinate is $pixel_\mathrm{q}(u_\mathrm{q}, v_\mathrm{q})$. According to Equation (1), the pixel coordinates of point p, q are shown in Equations (6) and (7). The projection slope k_m of the point-pair on the mask is $k_m = (u_\mathrm{p} - u_\mathrm{q}) / (v_\mathrm{p} - v_\mathrm{q})$.

$$v_\mathrm{p} = \frac{x_\mathrm{p} \cdot f_x}{z_\mathrm{p}} + c_x \; u_\mathrm{p} = \frac{y_\mathrm{p} \cdot f_y}{z_\mathrm{p}} + c_y \tag{6}$$

$$v_\mathrm{q} = \frac{(x_\mathrm{p} + l_\mathrm{p}) \cdot f_x}{z_\mathrm{p} + n_\mathrm{p}} + c_x \; u_\mathrm{q} = \frac{(y_\mathrm{p} + m_\mathrm{p}) \cdot f_y}{z_\mathrm{p} + n_\mathrm{p}} + c_y \tag{7}$$

The center point of the parallelogram diameter calculation region is denoted as p. The length of the long side of this region is set to twice the pixel value, corresponding to the design diameter (d_l) of the rebar, while the width is fixed at six pixels. A color transformation is applied within this region, whereby red pixels are converted to blue, and black pixels are converted to white.

Since the rebar mask predicted by K-Net and DeepLabV3+ models have strong continuity, the blue area in Figure 10 is continuous. So, there will be no isolated white pixels in the middle of the blue area. In this way, we can assume that as long as there are white pixels around the blue pixel, the pixel is considered to be the boundary of the rebar mask (such as the pixel set Green in Figure 10). The pixels $green(u, v)$ in the set Green have the following two characteristics: ① Due to the influence of other environmental factors such as reflection during the point cloud acquisition, some points do not collect the depth information (the 3D coordinates corresponding to the pixel are $(0, 0, 0)$). ② The pixel is not in the imaginary plane γ, but in the point cloud set of the bottom formwork or other layers of the rebar lattice. The above two situations will cause some pixels in the mask which are not to be directly used for the diameter calculation, so we need to assume that the point cloud corresponding to the green pixel is in the imaginary plane γ. As mentioned above, the plane γ is perpendicular to the plane formed by the rebar axis l_{rebar} and the origin O of the camera coordinate system, and the intersection of the two planes is the fitting line l_{rebar}. The foot of the perpendicular plane from the point O to the rebar axis l_{rebar} is $\mathrm{A}(x_A, y_A, z_A)$, and point A is in plane γ.

The plane equation is $a_\gamma x + b_\gamma y + c_\gamma z + d_\gamma = 0$ and the plane normal vector is $\vec{v_\alpha} = \vec{\mathrm{AO}}$, so then we get Equation (8):

$$a_\gamma = x_\mathrm{A}\ b_\gamma = y_\mathrm{A}\ c_\gamma = z_\mathrm{A}\ d_\gamma = -\left({x_\mathrm{A}}^2 + {y_\mathrm{A}}^2 + {z_\mathrm{A}}^2\right) \tag{8}$$

As shown in Figure 11, the projection of $green(u, v)$ in the plane γ is B, and the direction vector $\vec{v_\mathrm{B}}$ of line BO is shown in Equation (9):

$$\vec{v_\mathrm{B}} = \left(\frac{v_i - c_x}{f_x}, \frac{u_i - c_y}{f_y}, 1.0\right) \tag{9}$$

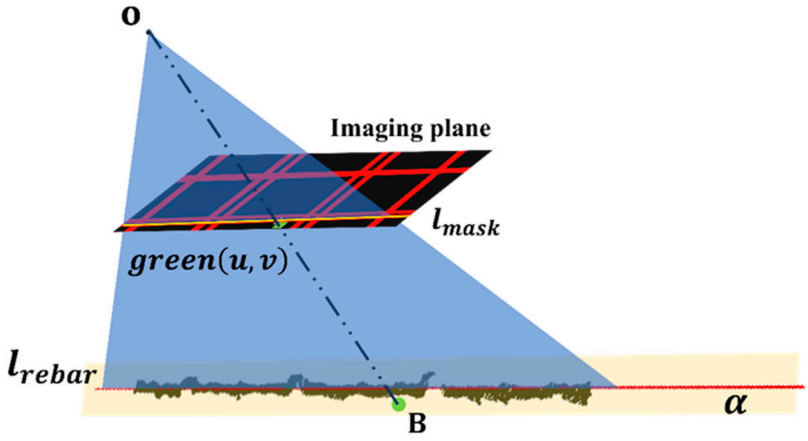

Figure 11. Projection geometry relationship.

Then obtain the intersection point $\mathrm{B}(x_\mathrm{B}, y_\mathrm{B}, z_\mathrm{B})$ of line BO and plane γ.

As shown in Figure 11, the yellow line l_m is the projection of the rebar axis l_{rebar} on the imaging plane. And l_m divides the green pixels to two parts; one part is above the l_m, the other is below the l_m. The projection points of the green pixels above the l_m in plane γ are $\mathrm{B}_u(u = 1, 2, 3\cdots)$, the ones below the l_m in plane γ are $\mathrm{B}_l(l = 1, 2, 3\cdots)$, and the rebar diameter is $D = min(|\vec{B_u B_l}|)$.

4. Verification with Examples and Discussion

The experimental component (Figure 12a) is a 2 m × 2 m double-layer bidirectional rebar tied on-site. The nominal diameter of the upper rebar lattice is 12 mm, the nominal diameter of the lower rebar lattice is 14 mm, and the designed binding spacing is 200 mm. We altered the thickness of the protective layer by adding spacers, setting them at 15 mm, 20 mm, and 25 mm, respectively. Additionally, we captured the data on the construction site, as shown in the Figure 12b, where the concrete cover thickness is 15 mm, the rebar diameter is 8 mm, and the rebar spacing is about 15 mm.

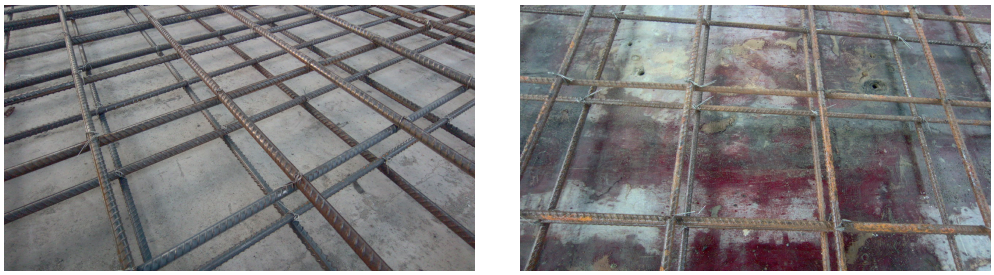

(**a**) Experimental component (**b**) Construction site

Figure 12. Data captured in two different conditions.

As shown in Figure 13, the data for the component were captured at points A, B, C, and D, located 400 mm, 500 mm, and 600 mm from the ground, respectively. To minimize the collection of extraneous data from distant rebar and ensure minimal obstruction between the upper and lower rebar lattices, the angle between the Z-axis of the camera coordinate system and the geographic coordinate system did not exceed 15° during the data acquisition process. Due to the inconvenience of the data capture at the construction site, data were only collected when located at about 500 mm.

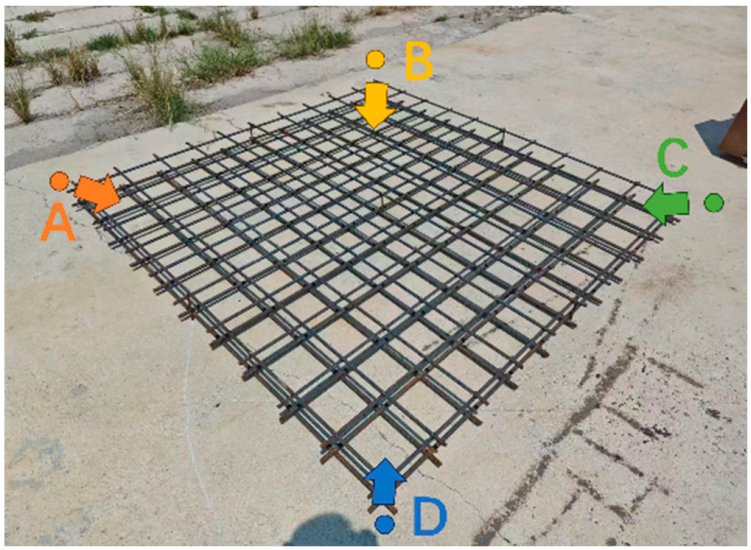

Figure 13. Data-captured position.

4.1. Detection of Concrete Cover Thickness and the Distance Between Upper and Lower Rebar Lattices

In Tables 4–6, the orange sections represent the results calculated from the data captured on the construction site, while the rest are the calculation results based on data from the experimental components.

Table 4. Concrete cover thickness and the distance between upper and lower rebar lattices' detection result.

h/mm	Concrete Cover Thickness				Distance Between Upper and Lower Lattices			
	Actual /mm	Detected /mm	Absolute Error/mm	Relative Error	Actual /mm	Detected /mm	Absolute Error/mm	Relative Error
400	15	14.59	0.41	2.7%	85	86.32	1.32	1.5%
	20	19.22	0.78	3.9%				
	25	23.57	1.43	5.7%				
500	15	14.66	0.34	2.3%	85	85.37	0.37	0.4%
	20	19.31	0.69	3.5%				
	25	23.82	1.18	4.7%				
	15	14.46	0.54	3.6%	54	53.55	0.45	0.8%
600	15	11.24	3.76	25.1%	85	87.22	2.22	2.6%
	20	17.41	2.59	18.5%				
	25	21.76	3.24	12.9%				

Table 5. Rebar spacing detection result.

h/mm	Rebar Lattice	Actual/mm	Detected (Absolute Error)/mm	Maximum of Relative Error/%
400	upper	194, 198	191 (−3), 201 (+3)	1.6
	lower	200, 199, 198, 201	198 (−2), 194 (−5), 200 (+2), 205 (+4)	2.5
500	upper	205, 194, 194, 198, 205	208 (+3), 192 (−2), 191 (−3), 199 (+1), 205 (0)	1.6
	lower	190, 203, 194, 195, 202	191 (+1), 200 (−3), 195 (+1), 191 (−4), 201 (−1)	2.1
	upper	149, 150, 148, 148	150 (+1), 149 (−1), 152 (+4), 149 (+1)	2.7
	lower	151, 153, 148, 149	150 (−1), 151 (−2), 150 (+2), 149 (0)	1.3
600	upper	188, 210, 205, 200, 205, 186	187 (+1), 211 (+1), 204 (−1), 200 (0), 203 (−2), 187 (+1)	1.0
	lower	199, 195, 202	196 (−3), 199 (+4), 202 (0)	2.0

Table 6. Rebar diameter measurement result.

Point	h/mm	Upper Rebar		Lower Rebar	
		Total	Wrong	Total	Wrong
A	400	3	0	5	0
	500	6	0	6	1
	600	5	0	5	0
B	400	4	0	5	0
	500	5	0	5	0
	600	6	0	7	0
C	400	4	0	5	0
	500	6	0	5	0
	600	6	0	6	0
D	400	4	0	5	0
	500	6	0	6	0
	600	5	0	5	1
Site	500	5	1	5	0
Total:		65	1	70	2
Accuracy:					97.8%

According to the algorithm flow in Section 3.1, calculate the concrete cover thickness and the distance between the upper and lower rebar lattices, and the results are shown in Table 4. When the capture distance is within 500 mm, the maximum absolute error of the covered thickness's measured value is 1.43 mm, and the relative error is less than 5.7%. However, when the measuring distance is greater than 500 mm, the absolute error of the cover thickness is 3.76 mm, and the relative error is 25.1%. When the capture distance is within 500 mm, the maximum absolute error of the measured value of the distance between the upper and lower rebar lattices is 1.32 mm, and the relative error is less than 1.5%. However, when the measuring distance is greater than 500 mm, the absolute error of the cover thickness is 2.22 mm, and the relative error is 2.6%. It can be found from Table 4 that the absolute error of the cover thickness is close to that of the distance between the two layers. This indicates that the error is caused by the inaccurate point cloud acquisition of the lower rebar lattice. The data inspection shows that the error is caused by the point cloud's low accuracy acquired at 600 mm.

4.2. Detection of Spacing of the Double-Layer Bidirectional Rebar

According to the algorithm flow in Section 3.2, calculate the data captured at point A; the results are shown in Table 5. The maximum absolute error of the rebar spacing is 5 mm and the maximum relative error is 2.7%. Compared with Section 4.1, the inaccuracy data acquisition of the lower rebar lattice will not affect the measurement of the rebar spacing. That is because the error in the depth (Z) direction only affects the measurement results in the X and Y directions a little. The error in the rebar spacing mainly comes from two aspects: ① The cross section of the point cloud used to fit the steel bar axis is the point cloud facing the camera rather than a complete circle. This will result in inaccurate rebar axis fitting. ② The measurement errors in the acquisition will also cause calculation errors.

4.3. Detection of Rebar Nominal Diameter

Based on the algorithmic procedure outlined in Section 3.3, the nominal diameter of the rebar was calculated at each detect-point. Figures 14 and 15, respectively, illustrate the calculated diameters for each rebar at all detect-points for the upper and lower layers at three different heights at Point A.

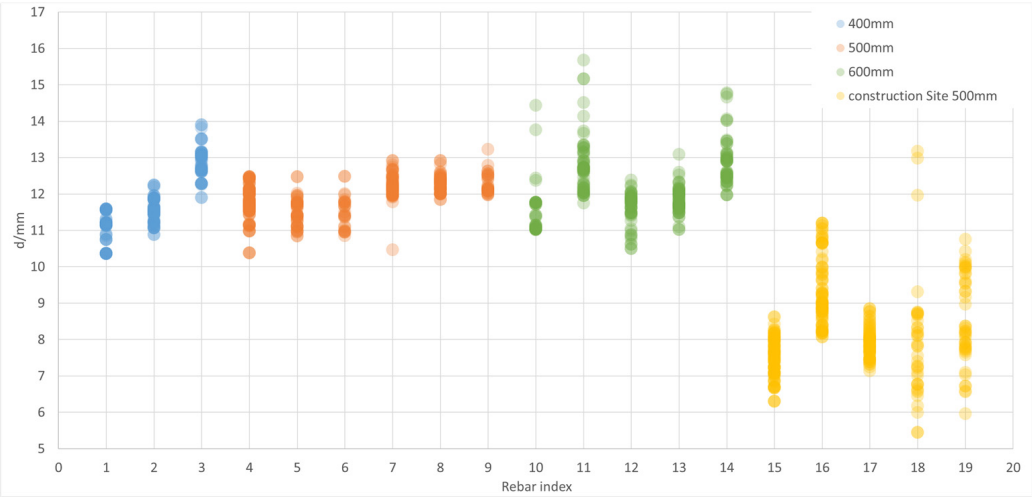

Figure 14. Upper rebar diameter measurement result for Point A and construction site.

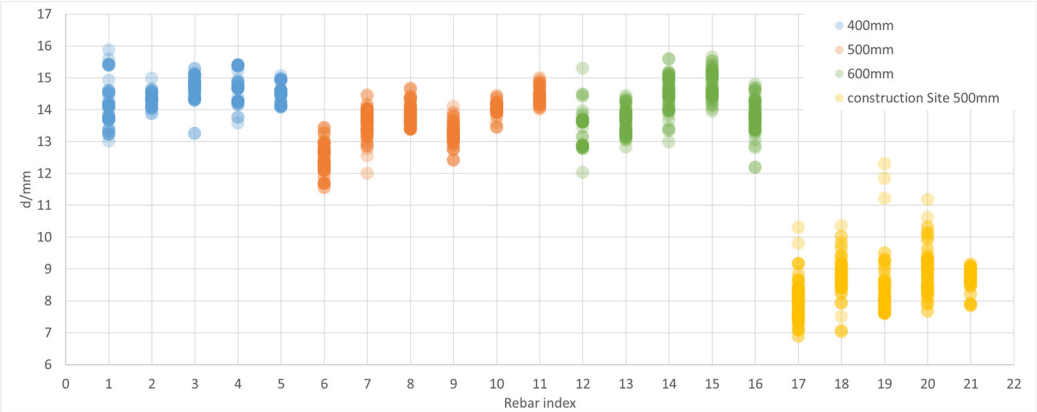

Figure 15. Lower rebar diameter measurement result for Point A and construction site.

Detect-points are uniformly selected along the length of the rebar axis, and diameter calculation regions are established near these detect-points according to the method outlined in Section 3.3. Among all detect-points for a given rebar, the number of points falling within 7–9, 9–11, 11–13, 13–15, and 15–17 is compared. If the highest number of points falls within the 7–9 range, the rebar nominal diameter is determined to be 8 mm. Similarly, ranges 9–11,11–13, 13–15, and 15–17 correspond to nominal diameters of 10 mm, 12 mm, 14 mm, and 16 mm, respectively.

As shown in Figure 14, among the 19 upper rebars, the calculation result for the sixteenth rebar did not match the actual nominal diameter. As shown in Figure 12b, it can be found that the rebars on the construction site were corroded. However, there are few similar images of the rebars in the RL-600 dataset, which result in the poor identification of the edges of the corroded rebars and lead to errors in the calculations. As for the third rebar, there were 37 points in the 11–13 mm range and 30 points in the 13–15 mm range, which are relatively close. As shown in Figure 15, among the 21 lower rebars, the calculation result for the sixth rebar did not match the actual nominal diameter. This discrepancy occurred because the rebar was in the shadow of the upper rebars, resulting in an indistinct edge of the rebar in the image and an erroneous prediction by the K-Net.

Through the above experiments, it can be found that both shadows and corrosion affect the clarity and accuracy of the rebar edges in the semantic segmentation mask. And this affects the calculation of the diameter of the rebar. Therefore, the dataset should be made with more complex scenarios, so that the semantic segmentation model can learn the relevant content and not forget it during the training process.

Table 6 presents the number of correctly detected rebar diameters at points A, B, C, and D, located at 400 mm, 500 mm, and 600 mm from the ground, as well as the data captured from the construction site. Due to the obstruction of the lower rebar caused by the upper rebar during data acquisition, such obstructed rebars were excluded from the analysis. The results indicate an accuracy rate of 98.4% for this inspection process, with a capture distance within 600 mm. Since nominal diameter errors for individual rebars are virtually nonexistent in actual engineering practice, this method adequately fulfils the requirements for rebar installation quality inspections in real-world applications.

5. Conclusions

This paper develops an automatic inspection workflow for the RC slab rebar installation quality based on RGB-D images captured by a structured light camera. It addresses the limitations of existing smart inspection processes by utilizing a more affordable and easily mountable structured light camera on mobile devices. This approach shifts from the traditional focus on semantic segmentation masks for single-layer mesh rebar inspections to using semantic information from point clouds as the primary basis for verification. A cohesive inspection system is established by integrating mask information and point cloud data through transformations between the camera and pixel coordinate systems.

The proposed automatic inspection process demonstrates performance metrics with a maximum absolute error of 1.43 mm and a relative error of less than 6% for concrete cover thickness measurements. The maximum absolute error for the distance between the upper and lower rebar lattices is 1.32 mm, with a relative error of 1.5%. The maximum absolute error for rebar spacing is 5 mm, with a maximum relative error of 2.7%. The accuracy of nominal rebar diameter verification is 97.8%. Both the inspection error and accuracy meet the requirements for practical engineering applications.

This technology enables comprehensive inspections of double-layer rebar lattices rather than just sampling checks, facilitates the non-contact inspection of the lower rebar, and simplifies the inspector's task. Additionally, it offers the potential for integration with drone technology, reducing the need for inspectors to climb unfinished structures, and can be linked to other applications for automatic report generation.

In future research, the combination of depth cameras and robots which can walk on the rebar lattices' bar can be considered. And then multi-view stitching can be used to form a globally visualization model. Additionally, it is necessary to upgrade the dataset established in this paper by adding more images with shadows and corroded rebars, in order to enhance the ability of distinguishing the shadow and rebars.

Author Contributions: Conceptualization, R.W. and H.Q.; Methodology, R.W., J.Z. and J.S.; Data curation, R.W.; Writing—original draft, R.W.; Supervision, H.Q. All authors have read and agreed to the published version of the manuscript.

Funding: This research received no external funding.

Data Availability Statement: Data is contained within the article.

Conflicts of Interest: The authors declare no conflict of interest.

References

1. O'Connor, M.; Stowe, J.; Potocnik, J.; Giannotti, N.; Murphy, S.; Rainford, L. 3D Virtual Reality Simulation in Radiography Education: The Students' Experience. *Radiography* **2021**, *27*, 208–214. [CrossRef] [PubMed]
2. Malamateniou, C.; Knapp, K.M.; Pergola, M.; Woznitza, N.; Hardy, M. Artificial Intelligence in Radiography: Where Are We Now and What Does the Future Hold? *Radiography* **2021**, *27*, S58–S62. [CrossRef] [PubMed]
3. Yue, S.; Zhang, Z.; Shi, Y.; Cai, Y. WGS-YOLO: A Real-Time Object Detector Based on YOLO Framework for Autonomous Driving. *Comput. Vis. Image Underst.* **2024**, *249*, 104200. [CrossRef]
4. Huo, R.; Chen, J.; Zhang, Y.; Gao, Q. 3D Skeleton Aware Driver Behavior Recognition Framework for Autonomous Driving System. *Neurocomputing* **2024**, *613*, 128743. [CrossRef]
5. Sabeti, S.; Ardecani, F.B.; Shoghli, O. Augmented Reality Safety Warnings in Roadway Work Zones: Evaluating the Effect of Modality on Worker Reaction Times. *Transp. Res. Part C Emerg. Technol.* **2024**, *169*, 104867. [CrossRef]
6. Arunjaroensuk, S.; Yotpibulwong, T.; Fu, P.-S.; Wang, J.-C.; Hung, C.-C.; Mattheos, N.; Pimkhaokham, A. Implant Position Accuracy Using Dynamic Computer-Assisted Implant Surgery (CAIS) Combined with Augmented Reality: A Randomized Controlled Clinical Trial. *J. Dent. Sci.* 2024; *in press*. [CrossRef]
7. Acke, L.; Corradi, D.; Verlinden, J. Comprehensive Educational Framework on the Application of 3D Technologies for the Restoration of Cultural Heritage Objects. *J. Cult. Herit.* **2024**, *66*, 613–627. [CrossRef]
8. Li, Q.; Yang, G.; Gao, C.; Huang, Y.; Zhang, J.; Huang, D.; Zhao, B.; Chen, X.; Chen, B.M. Single Drone-Based 3D Reconstruction Approach to Improve Public Engagement in Conservation of Heritage Buildings: A Case of Hakka Tulou. *J. Build. Eng.* **2024**, *87*, 108954. [CrossRef]
9. Yuan, X.; Smith, A.; Moreu, F.; Sarlo, R.; Lippitt, C.D.; Hojati, M.; Alampalli, S.; Zhang, S. Automatic Evaluation of Rebar Spacing and Quality Using LiDAR Data: Field Application for Bridge Structural Assessment. *Autom. Constr.* **2023**, *146*, 104708. [CrossRef]
10. Kim, M.-K.; Thedja, J.P.P.; Wang, Q. Automated Dimensional Quality Assessment for Formwork and Rebar of Reinforced Concrete Components Using 3D Point Cloud Data. *Autom. Constr.* **2020**, *112*, 103077. [CrossRef]
11. Chang, C.-C.; Huang, T.-W.; Chen, Y.-H.; Lin, J.J.; Chen, C.-S. Autonomous Dimensional Inspection and Issue Tracking of Rebar Using Semantically Enriched 3D Models. *Autom. Constr.* **2024**, *160*, 105303. [CrossRef]
12. Wang, Q.; Cheng, J.C.P.; Sohn, H. Automated Estimation of Reinforced Precast Concrete Rebar Positions Using Colored Laser Scan Data. *Comput.-Aided Civ. Infrastruct. Eng.* **2017**, *32*, 787–802. [CrossRef]
13. Peng, L.; Chao, W.; Shuangmiao, L.; Baocai, F. Research on Crack Detection Method of Airport Runway Based on Twice-Threshold Segmentation. In Proceedings of the 2015 Fifth International Conference on Instrumentation and Measurement, Computer, Communication and Control (IMCCC), Qinhuangdao, China, 18–20 September 2015; pp. 1716–1720.

14. Win, M.; Bushroa, A.R.; Hassan, M.A.; Hilman, N.M.; Ide-Ektessabi, A. A Contrast Adjustment Thresholding Method for Surface Defect Detection Based on Mesoscopy. *IEEE Trans. Industr. Inform.* **2015**, *11*, 642–649. [CrossRef]
15. Zhao, H.; Qin, G.; Wang, X. Improvement of Canny Algorithm Based on Pavement Edge Detection. In Proceedings of the 2010 3rd International Congress on Image and Signal Processing, Yantai, China, 16–18 October 2010; pp. 964–967.
16. Wang, Y.; He, Z.; Zeng, X.; Cen, Z.; Zeng, J.; Ren, X.; Cheng, X. Real-Time Spatial Contextual Network Based on Deep Learning for Bridge Exposed Rebar Segmentation. *Constr. Build. Mater.* **2024**, *449*, 138379. [CrossRef]
17. Mohamed, Y.S.; Shehata, H.M.; Abdellatif, M.; Awad, T.H. Steel Crack Depth Estimation Based on 2D Images Using Artificial Neural Networks. *Alex. Eng. J.* **2019**, *58*, 1167–1174. [CrossRef]
18. Cui, B.; Wang, C.; Li, Y.; Li, H.; Li, C. Application of Computer Vision Techniques to Damage Detection in Underwater Concrete Structures. *Alex. Eng. J.* **2024**, *104*, 745–752. [CrossRef]
19. Loverdos, D.; Sarhosis, V. Pixel-Level Block Classification and Crack Detection from 3D Reconstruction Models of Masonry Structures Using Convolutional Neural Networks. *Eng. Struct.* **2024**, *310*, 118113. [CrossRef]
20. Luo, R.; Zhou, Z.; Chu, X.; Ma, W.; Meng, J. 3D Deformation Monitoring Method for Temporary Structures Based on Multi-Thread LiDAR Point Cloud. *Measurement* **2022**, *200*, 111545. [CrossRef]
21. El-Din Fawzy, H.; Kandeel, R.; Farhan, M. Detection of Deformations in Reinforced Concrete Structures Using Modern Surveying Techniques. *Alex. Eng. J.* **2023**, *70*, 191–218. [CrossRef]
22. Díaz-Vilariño, L.; Conde, B.; Lagüela, S.; Lorenzo, H. Automatic Detection and Segmentation of Columns in As-Built Buildings from Point Clouds. *Remote Sens.* **2015**, *7*, 15651–15667. [CrossRef]
23. Zhao, W.; Jiang, Y.; Liu, Y.; Shu, J. Automated Recognition and Measurement Based on Three-Dimensional Point Clouds to Connect Precast Concrete Components. *Autom. Constr.* **2022**, *133*, 104000. [CrossRef]
24. Yu, J.; Shi, X.; Feng, Y.; Chang, J.; Liu, J.; Xi, H.; Huang, S.; Zhang, W. Machine Learning-Based Design and Optimization of Double Curved Beams for Multi-Stable Honeycomb Structures. *Extreme Mech. Lett.* **2023**, *65*, 102109. [CrossRef]
25. Kardovskyi, Y.; Moon, S. Artificial Intelligence Quality Inspection of Steel Bars Installation by Integrating Mask R-CNN and Stereo Vision. *Autom. Constr.* **2021**, *130*, 103850. [CrossRef]
26. Xin, J.; Akiyama, M.; Frangopol, D.M. Autonomous Detection of Steel Corrosion Spatial Variability in Reinforced Concrete Using X-Ray Technology and Deep Learning-Based Semantic Segmentation. *Autom. Constr.* **2024**, *158*, 105252. [CrossRef]
27. Xi, J.; Gao, L.; Zheng, J.; Wang, D.; Tu, C.; Jiang, J.; Miao, Y.; Zhong, J. Automatic Spacing Inspection of Rebar Spacers on Reinforcement Skeletons Using Vision-Based Deep Learning and Computational Geometry. *J. Build. Eng.* **2023**, *79*, 107775. [CrossRef]
28. Fischler, M.A.; Bolles, R.C. Random Sample Consensus. *Commun. ACM* **1981**, *24*, 381–395. [CrossRef]
29. Ronneberger, O.; Fischer, P.; Brox, T. U-Net: Convolutional Networks for Biomedical Image Segmentation. In *Medical Image Computing and Computer-Assisted Intervention–MICCAI 2015*; Springer: Cham, Switzerland, 2015; pp. 234–241.
30. Alharbi, A.H.; Aravinda, C.V.; Lin, M.; Venugopala, P.S.; Reddicherla, P.; Shah, M.A. Segmentation and Classification of White Blood Cells Using the UNet. *Contrast Media Mol. Imaging* **2022**, *2022*, 5913905. [CrossRef] [PubMed]
31. Du, X.-F.; Wang, J.-S.; Sun, W. UNet Retinal Blood Vessel Segmentation Algorithm Based on Improved Pyramid Pooling Method and Attention Mechanism. *Phys. Med. Biol.* **2021**, *66*, 175013. [CrossRef]
32. Liu, F.; Wang, L. UNet-Based Model for Crack Detection Integrating Visual Explanations. *Constr. Build. Mater.* **2022**, *322*, 126265. [CrossRef]
33. Zhang, L.; Shen, J.; Zhu, B. A Research on an Improved Unet-Based Concrete Crack Detection Algorithm. *Struct. Health Monit.* **2021**, *20*, 1864–1879. [CrossRef]
34. Yu, G.; Dong, J.; Wang, Y.; Zhou, X. RUC-Net: A Residual-Unet-Based Convolutional Neural Network for Pixel-Level Pavement Crack Segmentation. *Sensors* **2022**, *23*, 53. [CrossRef] [PubMed]
35. Zhang, W.; Pang, J.; Chen, K.; Loy, C.C. K-Net: Towards Unified Image Segmentation. *Adv. Neural Inf. Process. Syst.* **2021**, *34*, 10326–10338.
36. Chen, L.-C.; Zhu, Y.; Papandreou, G.; Schroff, F.; Adam, H. Encoder-Decoder with Atrous Separable Convolution for Semantic Image Segmentation. In Proceedings of the European Conference on Computer Vision (ECCV), Munich, Germany, 8–14 September 2018.
37. Hartigan, J.A.; Wong, M.A. Algorithm AS 136: A K-Means Clustering Algorithm. *Appl. Stat.* **1979**, *28*, 100. [CrossRef]